The Astrophysical Journal, 877:139 (13pp), 2019 June 1 https://doi.org/10.3847/1538-4357/ab1751

Constraining Strangeness in Dense Matter with GW170817

R. O. Gomes [1,2], P. Char[3,4], and S. Schramm[1]
[1] Frankfurt Institute for Advanced Studies, Frankfurt am Main, Germany; rosana.gomes@ufrgs.br
[2] Astronomy Department, Universidade Federal do Rio Grande do Sul (UFRGS), Porto Alegre, Brazil
[3] Inter-University Centre for Astronomy and Astrophysics, Post Bag 4, Ganeshkhind, Pune—411 007, India
[4] INFN Sezione di Ferrara, VIA Saragat 1, I-44100 Ferrara, Italy
Received 2018 June 20; revised 2019 March 11; accepted 2019 April 3; published 2019 June 4

Abstract

Particles with strangeness content are predicted to populate dense matter, modifying the equation of state of matter inside neutron stars as well as their structure and evolution. In this work, we show how the modeling of strangeness content in dense matter affects the properties of isolated neutron stars and the tidal deformation in binary systems. For describing nucleonic and hyperonic stars we use the many-body forces model at zero temperature, including the ϕ mesons for the description of repulsive hyperon–hyperon interactions. Hybrid stars are modeled using the MIT Bag Model with vector interaction (vMIT) in both Gibbs and Maxwell constructions, for different values of bag constant and vector interaction couplings. A parameterization with a Maxwell construction, which gives rise to a third family of compact stars (twin stars), is also investigated. We calculate the tidal contribution that adds to the post-Newtonian point-particle corrections, the associated love number for sequences of stars of different composition (nucleonic, hyperonic, hybrid, and twin stars), and determine signatures of the phase transition on the gravitational waves in the accumulated phase correction during the inspirals among different scenarios for binary systems. In light of the recent results from GW170817 and the implications for the radius of $\sim 1.4\,M_{\odot}$ stars, our results show that hybrid stars can only exist if a phase transition takes place at low densities close to saturation.

Key words: equation of state – gravitational waves – dense matter – stars: neutron

1. Introduction

At the core of neutron stars, densities many orders of magnitude higher than the ones measured in experiments on Earth can be reached. It is predicted that exotic degrees of freedom can also populate these objects, and that even the dissolution of baryons into their quark constituents through a phase transition to quark matter could be facilitated in such extreme environments. The impact of exotic compositions on the structure of isolated neutron stars has been studied in the past for stars composed of hyperons (Dexheimer & Schramm 2008; Gomes et al. 2015; Oertel et al. 2015; Chatterjee & Vidaña 2016; Mishra et al. 2016; Vidaña 2016; Yamamoto et al. 2016; Tolos et al. 2017a; Torres et al. 2017), Delta baryon resonances (Schurhoff et al. 2010; Drago et al. 2014, 2016; Cai et al. 2015; Zhu et al. 2016), meson condensates (Menezes et al. 2005; Alford et al. 2010; Fernandez et al. 2010; Mesquita et al. 2010; Mishra et al. 2010; Lim et al. 2014; Muto et al. 2015), quarks, or even color superconducting quark matter (Buballa et al. 2004; Alford et al. 2005; Bombaci et al. 2007; Bonanno & Sedrakian 2012; Alford & Sedrakian 2017). Such degrees of freedom are usually associated with a softening of the equation of state (EoS), impacting the maximum mass and stability of stars (Hempel et al. 2009; Klähn et al. 2013).

When hyperons are taken into account in relativistic mean field models, special attention must be given to the hyperon–hyperon interaction modeling due to their internal strangeness degree of freedom. This is done through the introduction of ϕ and σ^* mesons, which mediate the interaction among these particles by describing repulsion and attraction features, respectively (Schaffner & Mishustin 1996). The impact of the presence of hyperons on the EoS of dense matter has been widely discussed in the literature under the name of hyperon puzzle (Bednarek et al. 2012; Jiang et al. 2012; Colucci & Sedrakian 2013; Gomes et al. 2015; Oertel et al. 2015; Zhao 2015; Chatterjee & Vidaña 2016; Fortin et al. 2016; Bombaci 2017; Haidenbauer et al. 2017; Tolos et al. 2017a, 2017b; Torres et al. 2017; de Oliveira et al. 2018). In particular, these new degrees of freedom are responsible for the softening of the EoS, making it difficult to reproduce massive neutron stars without the need of extra ingredients in the models, such as the vector strange meson ϕ, a phase transition to quark matter at higher densities or quarkyonic matter (McLerran & Reddy 2018). So far, the scarce information regarding the hyperon-meson coupling, largely obtained by reproducing hyperon potentials deduced from experiment (Weissenborn et al. 2012; Gomes et al. 2015; Fortin et al. 2017; Sun et al. 2018), makes this topic still unresolved.

With respect to a possible quark phase in astrophysical environments, the indirect observation of the quark-gluon plasma in the regime of high temperatures and low densities in ultrarelativistic heavy-ion collisions is in accordance with the existence of quark matter at the beginning of the universe (Shuryak 2009). The general study of the QCD phase structure relates the fields of heavy-ion collisions and neutron stars, where both approaches cover complementary regimes of density and temperature. Here, the experimental efforts toward lower heavy-ion beam energies with rather large baryon densities at the future Facility for Antiproton and Ion Research (FAIR) and Nuclotron-based Ion Collider fAcility, and the conditions of the recently observed neutron star mergers might lead to overlapping conditions of density and temperature in heavy-ion collisions and merger events. However, the fact that the regime of (star-relevant) high densities and low temperatures cannot be accessed by lattice or perturbative calculations makes the quark matter EoS even less constrained than the hadronic one, where at least there is some information on ground state matter properties. For this reason, effective models are used, rendering the determination of the phase transition point extremely model dependent.

Hybrid stars have been applied to investigate a broad range of topics regarding compact stars, such as nucleation in hadronic matter (Bombaci et al. 2007, 2009, 2016), color superconductivity in quark matter (Buballa et al. 2004; Alford et al. 2005; Bombaci et al. 2007; Bonanno & Sedrakian 2012; Alford & Sedrakian 2017), stability (Buballa et al. 2004; Ippolito et al. 2008; Pereira et al. 2018), rotation of neutron stars (Glendenning et al. 1997; Chubarian et al. 2000; Glendenning & Weber 2001; Zdunik et al. 2006; Ippolito et al. 2008; Dimmelmeier et al. 2009; Ayvazyan et al. 2013; Bejger et al. 2017), magnetic neutrons stars (Rabhi et al. 2009; Franzon et al. 2015, 2016; Sotani & Tatsumi 2015), thermal evolution (Page et al. 2006; Dexheimer et al. 2013, 2015; de Carvalho et al. 2015), proto-neutron stars (Pons et al. 2001; Yasutake & Kashiwa 2009; Mariani et al. 2017), supernovae (Hempel et al. 2009; Heinimann et al. 2016), radial oscillations (Brillante & Mishustin 2014; Alford & Han 2016; Pereira et al. 2018), etc. The deconfinement phase transition has been extensively studied with different models such as Nambu-Jona-Lasinio (Yasutake & Kashiwa 2009; Lenzi & Lugones 2012; Klähn et al. 2013; Shao et al. 2013; Benic et al. 2015; Alvarez-Castillo et al. 2016b; Pereira et al. 2016; Ranea-Sandoval et al. 2016; Miyatsu et al. 2017), MIT bag model (Burgio et al. 2002; Alford et al. 2005; Bhattacharyya et al. 2010; Yasutake et al. 2011; Shao et al. 2012; Franzon et al. 2016; Pereira et al. 2018), quark-meson coupling models (Mishra et al. 2016; Whittenbury et al. 2016; Zacchi et al. 2016; Miyatsu et al. 2017), and other approaches (Dexheimer & Schramm 2010; Chen et al. 2011; Dexheimer et al. 2015; Li et al. 2015; Alvarez-Castillo et al. 2016a; Burgio & Zappalà 2016; Schramm et al. 2016), showing that the features of the models used to describe both phases have implications for the determination of the macroscopic properties and composition of stars.

Phase transitions taking place in neutron stars are usually described either in sharp or smooth scenarios: in the case of a sharp transition, a local charge neutrality is imposed in what is named a Maxwell construction; while in a Gibbs construction scenario a global charge neutrality takes place, generating a mixed phase structure (Glendenning 1992). However, which approach might be more realistic depends on poorly known strong interaction quantities like the QCD surface tension (w.g. Heiselberg et al. 1993; Alford et al. 2001; Voskresensky et al. 2003; Pinto et al. 2012; Stiele & Schaffner-Bielich 2016). Both scenarios have been applied to describe hybrid stars (Hempel et al. 2009; Yasutake & Kashiwa 2009; Alaverdyan et al. 2010; Bhattacharyya et al. 2010; Yasutake et al. 2011; Contrera et al. 2017), indicating that the internal composition of stars can change substantially. In particular, the occurrence of a sharp phase transition to quark matter can in some cases allow for the appearance of a third family of compact stars and, consequently, for twin star configurations in which two stars have the same gravitational mass but different radii and composition (Dexheimer et al. 2015; Alford & Han 2016; Alford & Sedrakian 2017; Ayriyan et al. 2017).

In this sense, observational data from neutron stars can better constrain the modeling of strangeness in dense matter and works as a powerful tool to address the hyperon puzzle, as well as the interaction among quarks in hybrid stars. Almost a decade ago, the observation of massive neutron stars imposed constraints on the EoS of nuclear and quark matter, indicating that repulsion must be strong enough to reach $\sim 2\,M_{\odot}$ (Demorest et al. 2010; Antoniadis et al. 2013). However, in a recent reanalysis also using Shapiro delay for determining the mass of pulsars, a smaller mass of $M = 1.928 \pm 0.017\,M_{\odot}$ (with 68.3% credibility) is estimated for the PSR J19180642 pulsar (Fonseca et al. 2016).

A further stellar property that is affected by possible exotic phases is the neutron star radius. The accuracy of radius determinations, which come from energy flux measurements including assumptions about the stellar atmosphere, is still quite limited. One of the current problems for acquiring such data is due to the impossibility of accurately measuring luminosity and distance of the stars separately. Furthermore, the temperature determination of these objects is complicated due to nonthermal emissions on their spectra arising from cyclotron radiation. For these reasons, values of neutron star radii have large error bars and substantial efforts are being made to obtain much improved results in the future, like the missions Neutron Star Interior Composition Explorer (NICER),[5] *Nuclear Spectroscopic Telescope Array* (*NuSTAR*)[6] and the Square Kilometer Array (SKA).[7]

The recent detection of gravitational wave (GW) events has started the multimessenger era in astrophysics, and due to the extremely compact nature of neutron stars, it has proven to be a superb tool for constraining the nuclear matter EoS (Abbott et al. 2017; Banik & Bandyopadhyay 2017). It is expected that more GW events will be detected with the new generation and forthcoming ground-based detectors such as aLIGO,[8] aVIRGO,[9] KAGRA,[10] and the proposed Einstein Telescope.[11]

In a coalescing binary neutron star system, stars exert a tidal force on each other and, when they are close enough, this tidal perturbation leads to a deformation on them. For this system, the imprint of this deformation can be clearly seen in the early inspiral stages of the GW signal. It modifies the waveform from the point-particle structure and results in a lag in the waveform phase. In particular, analysis from the first direct BNS GW event, the GW170817 event, detected from Advanced LIGO in 2017 (Abbott et al. 2017), pose new constraints on the tidal deformability features of neutron stars. From preliminar results for low spin systems, it is estimated that the dimensionless tidal deformability $\tilde{\Lambda}$ has upper and lower limits of $\tilde{\Lambda} < 800$–1000 (Abbott et al. 2017; De et al. 2018) and $\tilde{\Lambda} > 400$ (Radice et al. 2018), respectively, the latter one obtained by considering the substantial kilonova signal. In a recent reanalysis of the data by the LIGO collaboration a limit on $\tilde{\Lambda}$ was derived as $\tilde{\Lambda} = 300^{+420}_{-230}$ (Abbott et al. 2019). Assuming the validity of chiral effective field theory results for neutron matter up to 2 times saturation density, a range of $80 < \tilde{\Lambda} < 570$ was derived (Tews et al. 2018).

The phase correction due to tidal deformation is characterized by a single EoS-dependent parameter, the Love number k_2 of the NS (Love 1909), also associated to the tidal deformation parameter λ. Tidal effects in this part of the signal will result in a phase shift accumulated over the cycles, which comes from the deviation from the point particle post-Newtonian waveforms. This is defined as $\tilde{\lambda}$, the weighted average of the deformations of individual stars, and also depends on the chirp

[5] NICER: http://heasarc.gsfc.nasa.gov/docs/nicer/index.html.
[6] *NuSTAR*: https://www.nustar.caltech.edu.
[7] SKA: http://www.skatelescope.org.
[8] LIGO: http://www.ligo.caltech.edu.
[9] VIRGO: http://www.virgo.infn.it.
[10] Kagra: http://gwcenter.icrr.u-tokyo.ac.jp/en/
[11] ET: http://www.et-gw.eu/.

mass of the system. Therefore, a sufficiently large signal-to-noise ratio detection can be used to distinguish such corrections to the waveform to extract the EoS information. The understanding of tidal deformation in double neutron stars system has been a topic in the literature for a long time (Damour & Nagar 2009; Hinderer et al. 2010; Postnikov et al. 2010). In particular, because the detection of GWs from a double black hole system, more excitement about this topic took place, and more recent research has been performed in order to understand the composition of neutron stars (Alford & Sedrakian 2017; Banik & Bandyopadhyay 2017; Kumar et al. 2017; Marques et al. 2017; Alvarez-Castillo et al. 2018; Ayriyan et al. 2018; Burgio et al. 2018; Drago & Pagliara 2018; Most et al. 2018; Nandi & Char 2018; Rueda et al. 2018; Paschalidis et al. 2018) and also on constraining the nuclear matter EoS (Alford & Sedrakian 2017; Banik & Bandyopadhyay 2017; Annala et al. 2018; Drago et al. 2018; Krastev & Li 2018; Malik et al. 2018; Raithel et al. 2018; Zhou et al. 2018; Zhu et al. 2018).

In this work we aim for constraining the composition of neutron stars through the analysis of isolated and binary systems and the comparison within the new constraints from observational data. The hadronic phase (with nucleons, hyperons, and leptons) is described by the many-body forces model (MBF model), which simulates the effects of MBF via nonlinear scalar field contributions in the effective coupling (Gomes et al. 2015). For the quark phase,we use the MIT bag model with vector interaction contributions (vMIT). When hybrid stars are modeled, the two phases are connected through a first-order phase transition and, in order to search for signals for the deconfinement, we investigate Maxwell and Gibbs construction scenarios.

In the case of isolated stars, we explore the effects of different compositions on the properties of stars, focusing on how the modeling of interaction among particles with strangeness content (hyperons and quarks) impacts the phase transition scenario and, consequently, the radius of stars. We also identify the existence of a third family of compact stars when a sharp phase transition takes place. For binary systems, we use a post-Newtonian approximation to calculate the structure of tidally deformed stars, in order to constrain the composition of neutron stars, as the comparatively cleaner signal from the early inspiral stage of the merger can present a detectable tidal signature (Flanagan & Hinderer 2008). Furthermore, due to the difference in radius for twin stars, we use the accumulated phase (sensitive to the fifth power of the radius) in order to identify a signal to distinguish these stars.

The article is organized as follows: In Section 2 we present the two models used for describing the EoS of matter inside stars, as well as the Maxwell and Gibbs construction formalisms. Section 3 is dedicated to the formalism used for describing binary systems in a post-Newtonian approximation and in Section 4, we discuss the results for isolated and binary systems. Finally, in Section 5, discussion and perspectives are presented.

2. Equation of State

In this section, we present the MBF model and the MIT bag model with vector interaction (vMIT) used to describe the hadronic and quark matter in our analysis, respectively. The two phases are connected by a first-order phase transition and modeled both in a Maxwell and a Gibbs construction.

2.1. Hadronic Phase

The MBF model (Gomes et al. 2015) is a relativistic mean field model in which meson field dependences are introduced in the couplings of baryons to mesons. The Lagrangian density of the MBF model reads:

$$\begin{aligned}\mathcal{L} = &\sum_b \overline{\psi}_b[\gamma_\mu(i\partial^\mu - g_{\omega b}\omega^\mu - g_{\varrho b}I_{3b}\varrho_3^\mu) - m_{b\zeta}^*]\psi_b \\ &+ \left(\frac{1}{2}\partial_\mu\sigma\partial^\mu\sigma - m_\sigma^2\sigma^2\right) + \frac{1}{2}\left(-\frac{1}{2}\omega_{\mu\nu}\omega^{\mu\nu} + m_\omega^2\omega_\mu\omega^\mu\right) \\ &+ \frac{1}{2}\left(-\frac{1}{2}\boldsymbol{\varrho}_{\mu\nu}.\boldsymbol{\varrho}^{\mu\nu} + m_\varrho^2\boldsymbol{\varrho}_\mu.\boldsymbol{\varrho}^\mu\right) + \left(\frac{1}{2}\partial_\mu\boldsymbol{\delta}.\partial^\mu\boldsymbol{\delta} - m_\delta^2\boldsymbol{\delta}^2\right) \\ &+ \frac{1}{2}\left(-\frac{1}{2}\phi_{\mu\nu}\phi^{\mu\nu} + m_\phi^2\phi_\mu\phi^\mu\right) + \sum_l \overline{\psi}_l\gamma_\mu(i\partial^\mu - m_l)\psi_l,\end{aligned} \tag{1}$$

where b and l correspond to the degrees of freedom of baryons (n, p, Λ, Σ^+, Σ^0, Σ^-, Ξ^0, Ξ^-) and leptons (e^-, μ^-), respectively. The scalar mesons σ and δ account for the description of attraction among baryons, while repulsion is described by the vector mesons ω, ϱ, and ϕ. Note that the ϕ mesons mediate interaction among hyperons, providing extra repulsion, which plays an important role in the description of massive stars with hyperon content (Schaffner & Mishustin 1996). For more about the properties of baryons, leptons, and mesons in this work, see Gomes et al. (2015).

The MBF contribution is introduced in the coupling of scalar fields as:

$$g_{ib}^* = \left(1 + \frac{g_{\sigma b}\sigma + g_{\delta b}I_{3b}\delta_3}{\zeta m_b}\right)^{-\zeta} g_{ib}, \tag{2}$$

for $i = \sigma$, δ, directly affecting the effective masses of baryons and, consequently, their chemical potentials. The field dependence in the couplings is, hence, introduced as a medium effect and is controlled by the ζ parameter, impacting directly on the effective mass of baryons: $m_b^* = m_b - g_{\sigma b}^*\sigma - g_{\delta b}^*I_3 b\delta_3$. This parameter can be associated to nonlinear terms that appear if one expands the term in Equation (2).

As strangeness is not conserved inside neutron stars due to the fact that typical timescales are much longer than the one for weak interaction, we allow for the appearance of hyperon degrees of freedom in our calculations. We model the coupling of hyperons using the SU(6) spin-flavor symmetry (Dover & Gal 1985; Schaffner et al. 1994), and also by fixing the hyperon potentials as $U_\Lambda^N = 28$ MeV, $U_\Sigma^N = +30$ MeV, and $U_\Xi^N = 18$ MeV (see Gomes et al. 2015 for other choices of hyperon potentials).

The MBF model reproduces both nuclear matter properties at saturation and the observational properties of neutron stars with hyperons (Gomes et al. 2015) and magnetic hybrid stars (Franzon et al. 2016; Dexheimer et al. 2017). For this work, the following nuclear properties at saturation were used: binding energy per nucleon $B/A = -15.75$ MeV, saturation density $\rho_0 = 0.15$ fm^{-3}, symmetry energy and its slope $a_{\rm sym}^0 = 32$ MeV and $L_0 = 97$ MeV, respectively.

2.2. Quark Phase

The quark matter is described by the MIT bag model with vector interaction contributions (vMIT). The Lagrangian density of the model reads:

$$\mathcal{L} = \sum_q [\overline{\psi}_q (i\gamma_\mu \partial^\mu - g_{Vq}\gamma_\mu V^\mu - m_q - B)\psi_q]\theta_H + \sum_l \overline{\psi}_l \gamma_\mu (i\partial^\mu - m_l)\psi_l, \quad (3)$$

where we consider the u, d, and s quarks and e^- and μ^- as leptons, labeled by the subscripts q and l, respectively. Also in this expression B denotes the bag constant and θ_H is the Heaviside step function that allows for a confinement/deconfinement feature of the model ($\theta_H = 1$ inside the bag; $\theta_H = 0$ outside) (Farhi & Jaffe 1984).

The vector interaction is introduced via the coupling of a vector-isoscalar meson V^μ to the quarks (with coupling constant g_V). Such a field is analogous to the ω field in hadronic models (Shao et al. 2013) and has a direct impact on the chemical potential of quarks, i.e., on the equilibrium conditions as:

$$\mu_q^* = \sqrt{(k_{F,q})^2 + (m_q)^2} + g_{Vq} V, \quad (4)$$

where $k_{F,q}$ and (m_q) are, respectively, the Fermi momenta and bare masses of quarks. Also, due to the beta equilibrium condition, the chemical potentials of quarks are related as $\mu_s = \mu_d = \mu_u + \mu_e$ and $\mu_u = \frac{1}{3}\mu_n - \frac{2}{3}\mu_e$, meaning that both hadronic and quark phases can be determined from the chemical potentials of neutrons and electrons.

It has been shown that vector interaction contributions in the description of quark matter plays a crucial role in the description of massive hybrid stars in agreement with observational data (Bonanno & Sedrakian 2012; Shao et al. 2012; Denke & Pinto 2013; Masuda et al. 2013; Contrera et al. 2014, 2017; Menezes et al. 2014; de Carvalho et al. 2015; Klähn & Fischer 2015; Ranea-Sandoval et al. 2016). These contributions have been investigated for different quark models (Contrera et al. 2014; Klähn & Fischer 2015; Ranea-Sandoval et al. 2016), and applied to neutron star studies (Shao et al. 2012; Denke & Pinto 2013; Contrera et al. 2014; Menezes et al. 2014; de Carvalho et al. 2015). In particular, we point out that the approach for describing quark matter with vector interactions used in this work is equivalent to the ones in Alford et al. (2005), Weissenborn et al. (2011), and Klähn & Fischer (2015), and referred to also as the vBag-model.

Although attempts to constrain the value of the vector interaction coupling have been made (for example, by incorporating higher orders of perturbation theory and radiative corrections; Fraga et al. 2001, 2014; Restrepo et al. 2015), this quantity remains widely uncertain. In order to investigate the impact of vector interactions in hybrid stars, we vary the coupling constant value and adopt the following set of parameters: $m_u = m_d = 1$ MeV, $m_s = 100$ MeV, $a_0 = (g_V/m_\omega) = 1.8$, 2.0, 2.2 fm^{-2}, $m_\omega = 782$ MeV, and $B^{1/4} = 170$ MeV.

2.3. Phase Transition

In the zero temperature regime present inside neutron stars, it is predicted that a first-order phase transition from hadronic to a deconfined quark matter takes place at high chemical potentials (baryon densities). In order to cover a wide range of scenarios, we investigate hybrid stars both with Gibbs and Maxwell constructions.

In a Gibbs construction the interface between the two phases is smoother, allowing for a mixed phase to appear. The mixed phase is constructed under the assumption of global charge neutrality, which leads to a charge rearrangement in both phases. On the other hand, a first-order phase transition described in a Maxwell construction has a sharp interface and, in order to guarantee the electric charge neutrality in the system, local charge neutrality is imposed in both phases separately.

The Maxwell criteria for zero temperature system reads (for both constructions):

$$P_H = P_Q, \qquad \mu_n^H = \mu_n^Q, \quad (5)$$

where $P_H(P_Q)$ and $\mu_n^H(\mu_n^Q)$ stand for the pressures and chemical potentials in the hadronic (quark) phase, respectively.

The chemical equilibrium condition determines the coexistence phase and the way that the charge conservation is introduced in the system has a direct impact on the pressure behavior at the transition point. When a local charge neutrality is imposed, the pressure depends only on the baryon chemical potential ($P_H(\mu_n)$, $P_Q(\mu_n)$) and is constant along the phase transition as a consequence of the Maxwell criteria. However, in a Gibbs construction scenario in which charge neutrality is global, the pressure depends both on the electrical and baryon chemical potentials ($P_H(\mu_n, \mu_e)$, $P_Q(\mu_n, \mu_e)$). This extra degree of freedom allows the pressure to vary as a function of the baryon chemical potential and still obey the pressure equality condition in both phases.

The comparison of both scenarios in the investigation of hybrid stars has been studied in several works, see, e.g., Bhattacharyya et al. (2010), Hempel et al. (2009), Yasutake & Kashiwa (2009), Yasutake et al. (2011), and Alaverdyan et al. (2010), where essentially the surface tension between the two phases determines which scenario is more appropriate. The threshold value for the surface tension has been calculated in several works (Alford et al. 2001; Voskresensky et al. 2003; Maruyama et al. 2007, 2008; Palhares & Fraga 2010; Pinto et al. 2012; Garcia & Pinto 2013; Lugones et al. 2013; Yasutake et al. 2016; Lugones & Grunfeld 2017), indicating that values are high and more compatible with a Maxwell construction.

In particular, a minimal threshold of $\sigma \sim 40$ MeV fm^{-2} (Endo et al. 2006; Yasutake et al. 2014) for this construction was estimated. However, such estimates depend strongly on the EoS (see Voskresensky et al. 2003), leaving the correct treatment of the phase transition as still an open question.

3. Love Number and Tidal Deformation

We follow the perturbation scheme developed in Flanagan & Hinderer (2008), Hinderer (2008), and Hinderer et al. (2010) to compute the tidal deformability and the associated Love number. If a static spherically symmetric star of mass M and radius R is placed in a time-independent external tidal field $\mathcal{E}_{ij}$, a quadrupole moment Q_{ij} is induced onto the star and to linear order, they satisfy the relation

$$Q_{ij} = -\lambda \mathcal{E}_{ij}, \quad (6)$$

where λ is defined as the tidal deformation parameter. It is related to the $l =$ two-dimensionless Love number k_2, which is

associated with the most dominant contribution to the stellar deformation as

$$\lambda = \frac{2}{3}k_2 R^5. \tag{7}$$

We consider only the leading order ($l = 2$), static perturbation, which is axisymmetric ($m = 0$) around the line joining the stars. The perturbed metric in Regge–Wheeler gauge (Regge & Wheeler 1957) can be written as (Hinderer et al. 2010)

$$\begin{aligned} ds^2 = &-e^{2\nu(r)}[1 + H(r)Y_{20}(\theta, \phi)]dt^2 \\ &+ e^{2\kappa(r)}[1 - H(r)Y_{20}(\theta, \phi)]dr^2 \\ &+ r^2[1 - K(r)Y_{20}(\theta, \phi)](d\theta^2 + \sin^2\theta d\phi^2), \end{aligned} \tag{8}$$

where, $K(r)$ and $H(r)$ are the perturbed metric functions related by $K'(r) = H'(r) + 2H(r)\Phi'(r)$. Substituting the fluid perturbations, $\delta T_0^{\ 0} = -\delta\epsilon(r)Y_{20}(\theta, \phi)$ and $\delta T_i^{\ i} = \delta p(r)Y_{20}(\theta, \phi)$, one obtains the equation for the function $H(r)$ (Hinderer et al. 2010)

$$\begin{aligned} &\left(-\frac{6e^{2\kappa}}{r^2} - 2(\nu')^2 + 2\nu'' + \frac{3}{r}\kappa' \right. \\ &\quad \left. + \frac{7}{r}\nu' - 2\nu'\kappa' + \frac{f}{r}(\nu' + \kappa')\right)H \\ &+ \left(\frac{2}{r} + \nu' - \kappa'\right)H' + H'' = 0, \end{aligned} \tag{9}$$

where, ϵ is the energy density and p is the pressure and, $f = d\epsilon/dp$. To calculate the tidal deformation, Equation (9) is to be solved simultaneously with the TOV equations

$$e^{2\kappa} = \left(1 - \frac{2m}{r}\right)^{-1}, \tag{10}$$

$$\frac{d\nu}{dr} = -\frac{1}{\epsilon + p}\frac{dp}{dr}, \tag{11}$$

$$\frac{dp}{dr} = -(\epsilon + p)\frac{m + 4\pi r^3 p}{r(r - 2m)}, \tag{12}$$

$$\frac{dm}{dr} = 4\pi r^2 \epsilon. \tag{13}$$

Here, $m = m(r)$ is the enclosed mass at radius r from the center. We take the radius of star R where $p(R) = 0$ and the mass of the star $M = m(R)$. The second-order differential equation for $H(r)$ can be rewritten as two coupled first-order differential equations and substituting the equlibrium metric functions using the TOV equations, taking the form

$$\frac{dH}{dr} = Z \tag{14}$$

$$\begin{aligned} \frac{dZ}{dr} = &2\left(1 - 2\frac{m}{r}\right)^{-1} H\left\{-2\pi[5\epsilon + 9p + f(\epsilon + p)] + \frac{3}{r^2}\right. \\ &\left. + 2\left(1 - 2\frac{m}{r}\right)^{-1}\left(\frac{m}{r^2} + 4\pi r p\right)^2\right\} \\ &+ \frac{2Z}{r}\left(1 - 2\frac{m}{r}\right)^{-1}\left\{-1 + \frac{m}{r} + 2\pi r^2(\epsilon - p)\right\}. \end{aligned} \tag{15}$$

The system is then solved radially outward from the center to the surface and matched with the exterior solution at the surface. The love number k_2 is given by

$$\begin{aligned} k_2 = &\frac{8C^5}{5}(1 - 2C)^2[2 + 2C(y - 1) - y] \\ &\times \{2C[6 - 3y + 3C(5y - 8)] \\ &+ 4C^3[13 - 11y + C(3y - 2) + 2C^2(1 + y)] \\ &+ 3(1 - 2C)^2[2 - y + 2C(y - 1)]\ln(1 - 2C)\}^{-1}, \end{aligned} \tag{16}$$

where a quantity $y = \frac{R\,Z(R)}{H(R)}$ is introduced and $C = \frac{M}{R}$ is the compactness of the star.

The observable signature of relativistic tidal deformation will have an imprint of the phase evolution of the GW spectrum of a binary NS system. To calculate the phase evolution for different EoS's, we again follow the formalism used by Hinderer et al. (2010), which shows in the secular limit, where the orbital period is much less than the gravitational radiation reaction timescale, that the tidal correction term adds linearly to the leading order post-Newtonian point particle corrections. Also, the signal will have cumulative effects of deformation coming from both the stars. Therefore, it is calculated from the weighted average of quadrupolar responses for the stars in a quasi-circular orbit, given by

$$\tilde{\lambda} = \frac{1}{26}\left[\frac{M_1 + 12M_2}{M_1}\lambda_1 + \frac{M_2 + 12M_1}{M_2}\lambda_2\right], \tag{17}$$

where, λ_1 and λ_2 are the tidal deformations of stars with masses M_1 and M_2. Finally, the tidal correction term to the phase evolution is given by

$$\delta\Psi^{\rm tidal} = -\frac{117\tilde{\lambda}x^{5/2}}{8\eta M_{\rm total}^5}, \tag{18}$$

where $M_{\rm total} = M_1 + M_2$ is the total mass of the binary, $x = (\omega M_{\rm total})^{2/3}$ is a dimensionless post-Newtonian parameter, and $\eta = M_1 M_2 / M_{\rm total}^2$ is the symmetric mass ratio. We also use the dimensionless tidal deformability Λ in our calculations, defined as $\Lambda = \lambda/M^5$. Similarly, Equation (17) can be recast following (Favata 2014) as

$$\begin{aligned} \tilde{\Lambda} &\equiv 32\frac{\tilde{\lambda}}{M_{\rm total}^5} \\ &= \frac{16}{13}\frac{(M_1 + 12M_2)M_1^4\Lambda_1 + (M_2 + 12M_1)M_2^4\Lambda_2}{(M_1 + M_2)^5}. \end{aligned} \tag{19}$$

4. Analysis and Discussion

In this section we discuss the impact of different neutron star compositions on the properties of isolated and binary star systems. The analysis was carried out using the models presented in Section 2, for nucleonic (Set 1), hyperonic (Set 2), and hybrid stars in Gibbs (Sets 3–5) and Maxwell (Sets 6–9) constructions.

For hadronic matter, we use two parameterizations of the MBF model, $\zeta = 0.040,\ 0.085$, which are able to describe nuclear properties at saturation and, in particular, have a compressibility $K_0 = 297,\ 225$ MeV, respectively (Gomes et al. 2015). When hyperons are allowed, ϕ mesons are

Table 1
Sets of Parameters Used in the Analysis, Where Y Stands for Hyperons (Λ, Σ, Ξ) and Q Stands for Quarks (u, d, s)

Set	Composition	Strangeness Modeling	$B^{1/4}$ (MeV)	a_0 (fm^2)	ζ
1	n, p, e, μ	n.a.	n.a.	n.a.	0.040
2	n, p, Y, e, μ	Y-Y int. (ϕ)	n.a.	n.a.	0.040
3	n, p, Y, e, μ, Q	Gibbs	160	1.8	0.085
4	n, p, Y, e, μ, Q	Gibbs	170	1.8	0.040
5	n, p, Y, e, μ, Q	Gibbs	170	2.2	0.040
6	n, p, Y, e, μ, Q	Maxwell	160	1.8	0.085
7	n, p, Y, e, μ, Q	Maxwell	170	1.8	0.040
8	n, p, Y, e, μ, Q	Maxwell	170	2.2	0.040
9	n, p, e, μ, Q	Maxwell	171	1.7	0.040

Note. The columns are (when applicable) name of the set, particles population, strangeness modeling, bag constant B, and vector interaction parameter a_0.

Table 2
Information About the Critical Strangeness Point (Due to Hyperons or Quarks) and Properties of Stars for the Different Sets of Parameters

Set	$\mu_{n,c}$ (MeV)	M_c ($M_\odot$)	$M_{\max}$ ($M_\odot$)	$R_{1.4\,M_\odot}$ (km)
1	n.a.	n.a.	2.57	14.44
2	1122	1.50	2.15	14.44
3	976	0.36	1.97	12.32
4	1038	0.98	2.04	14.02
5	1058	1.15	2.14	14.30
6	1058	1.03	1.99	12.87
7	1260	1.96	2.01	14.44
8	1638	2.15	2.15	14.44
9	1232	1.97	1.97 (N) 1.98 (Q)	14.44

Note. The columns are name of the set, critical chemical potential (μ_c), critical (M_c) and maximum ($M_{\max}$) mass of hybrid stars, and the radius of the $M = 1.4\,M_\odot$ star, respectively.

introduced in the calculations. We have chosen not to consider the minor contributions of the scalar meson σ^* in our calculations, as we are interested in massive neutron stars.

For both Gibbs and Maxwell constructions, we vary the values of the bag constant and vector coupling strengths in the ranges $B^{1/4} = 160{,}170$ MeV and $a_0 = 1.8,\ 2.2$ fm^2, respectively. For a Maxwell construction, we also identify a third family configuration of stars (twin stars) for the parameterization $B^{1/4} = 171$ MeV and $a = 1.7$ fm^2, which is present in the sets of our analysis. The choice of parameters for both phases allows for a description of symmetric nuclear matter in terms of a pure hadronic phase at low densities, and the regime of high densities to be described by a quark phase. All sets of parameters used in this work are summarized in Table 1.

4.1. Isolated Hybrid Stars

The features of phase transitions are directly affected by the stiffness of the EoS in both hadronic and quark phases. Therefore, the modeling of particles with nonzero strangeness interaction (hyperons and quarks) plays an important role in the properties of hybrid stars described within this framework. Table 2 summarizes this impact from both microscopic (EoS) and macroscopic (stars properties) points of view, for all sets of parameters used in our analysis.

First, comparing Sets 1 and 2 from Table 2, one can see that the introduction of hyperons in a hadronic model Set 2 softens drastically the EoS of hadronic matter, generating a sequence of stars with much smaller maximum mass, as discussed several times in the literature. For the same reason, as hyperons start to populate the core of stars, for masses above $1.5\,M_\odot$, the stars become more compact, i.e., present a smaller radius. Similarly, comparing hadronic stars, composed of nucleons, hyperons, and leptons (Sets 1 and 2) to all hybrid ones, containing a quark core (Sets 3–9), one can see a reduction in radius of 14.44–12.32 km (Set 3) for the $1.4\,M_\odot$ star due to the presence of quarks, for example.

Hybrid stars modeled under the assumption of a Gibbs construction (Sets 3–5) lead to a phase transition at low chemical potentials because of an extensive mixed phase. The critical chemical potentials range 976–1058 MeV, depending on the stiffness of the EoS used. From the comparison of Sets 3 and 4, we see that softer hadronic EoS lead to an earlier phase transition (lower $\mu_{n,c}$), as lower values of the ζ parameter (Set 4) in the MBF model generate a stiffer EoS due to weaker shielding of the scalar couplings of the model (Gomes et al. 2015). Equivalently, Sets 4 and 5 show that a softer quark EoS also results in a lower $\mu_{n,c}$, but here this behavior is caused by the strength of the vector interaction coupling. The critical masses for the onset of the appearance of quarks ranges between 0.36 and $1.15\,M_\odot$, indicating that it is possible to obtain low mass and more compact hybrid stars for such construction.

For the parameterization of the MBF model used in the analysis of Sets 3–5, a small fraction of Λ hyperons populate these stars because of global conservation conditions imposed in a Gibbs construction. In particular, the mixed phase covers a broad range of densities, implying that all stars present in this analysis have an incomplete phase transition to quark matter and, therefore, a core composed of a mixture of nucleons, Λ hyperons, leptons, and quarks.

For the corresponding stars modeled in a Maxwell construction (Sets 6–8), the phase transition takes place for chemical potentials higher than the ones in a Gibbs construction, and consequently the gap between critical and maximum masses is smaller. For this case, stars are mostly hadronic, containing only a small quark core. In particular, the critical and maximum masses are the same for Set 8, indicating that all stars in this family are hadronic and correspond to Set 2, as the phase transition never takes place for stable stars.

Moreover, after a scan of different parameterizations of the quark model, we identify in Set 9 a third family of stars. From Table 2, one can see that the critical chemical potential is slightly lower in comparison to other sets described by a Maxwell construction (Sets 7–8), which is associated to the lower value of the vector interaction coupling. However, the transition occurs for a baryon density of $\rho_{b,i} = 0.382$ fm^{-3}, ensuring that hyperons are present in the core of stars. For this configuration, the critical mass of $1.97\,M_\odot$ corresponds to the maximum mass of the first branch (denoted by N, for nucleonic stars). For higher densities, a phase of instability takes place until a stable branch of hybrid stars rises for a mass of $1.968\,M_\odot$, growing to a maximum mass of $1.978\,M_\odot$ (denoted by Q, for stars with a quark core).

In order to visualize the microscopic and macroscopic differences between these constructions, in Figure 1 we show the EoS (top) and the mass–radius diagrams (bottom) for all sets of parameters. The different approaches directly affect the

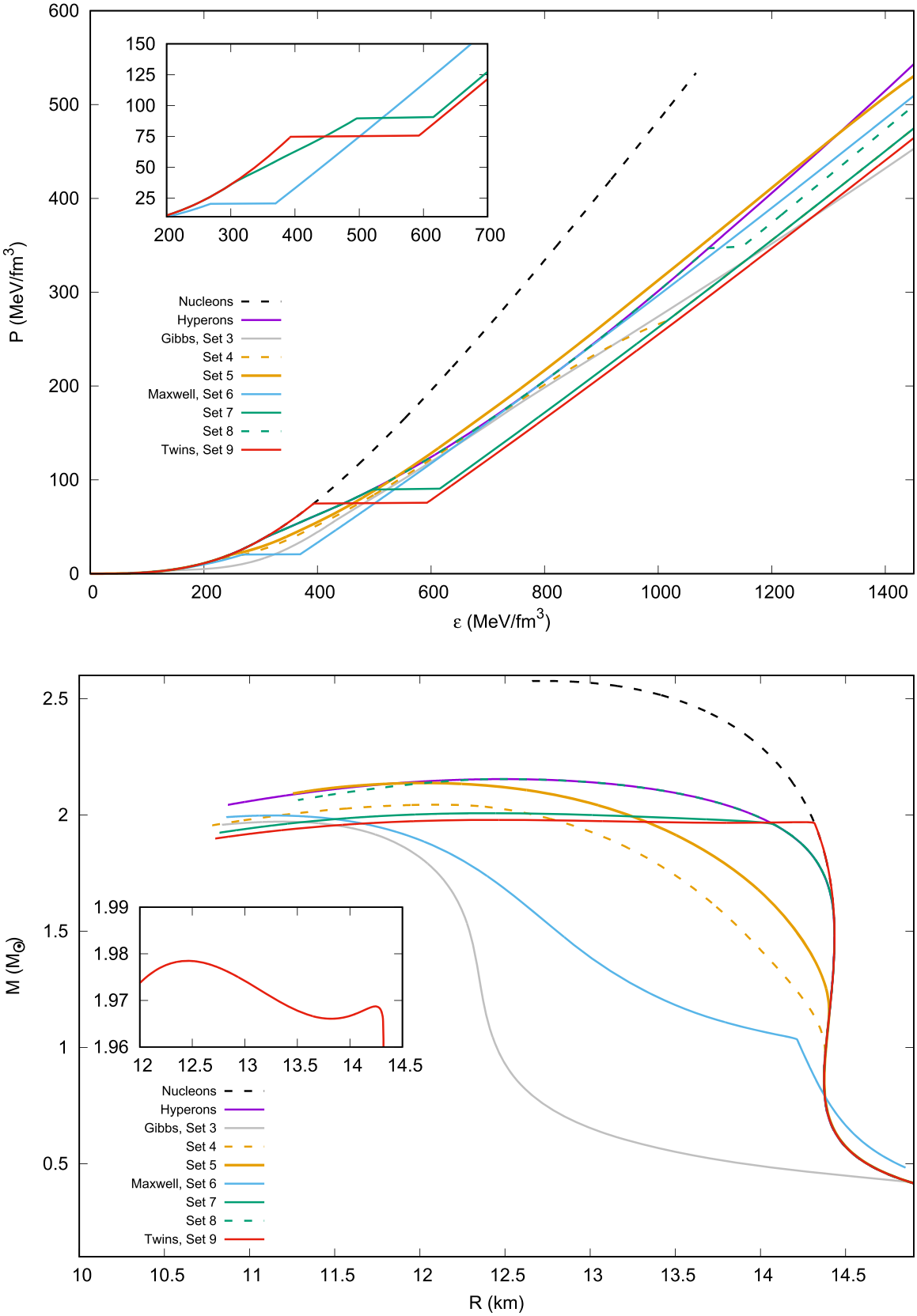

Figure 1. Equation of state (top) and mass–radius relation (bottom) for all parameterizations listed on Table 1. The curve in red (Set 9) shows a third family of stars configuration.

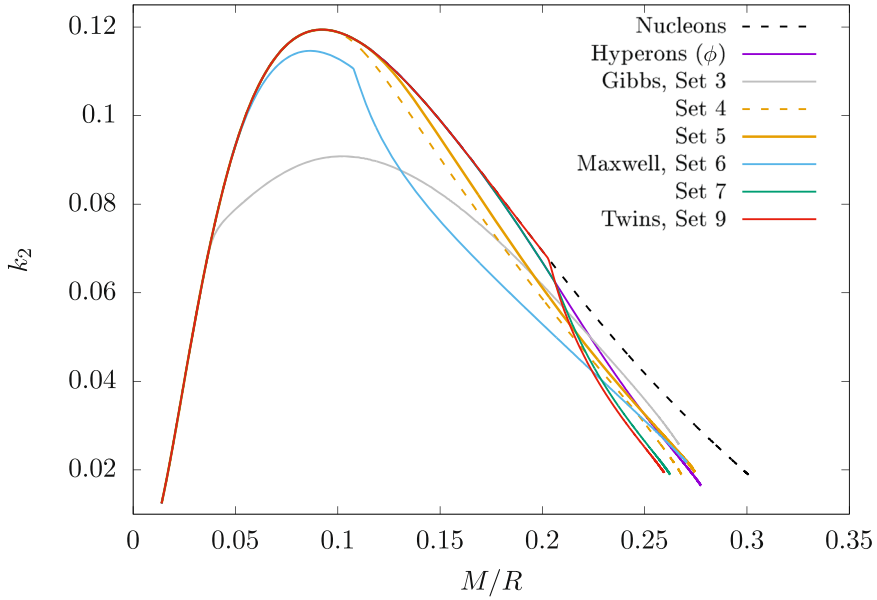

Figure 2. Love number (vertical axis) as a function of compactness (horizontal axis) for different sets of parameters.

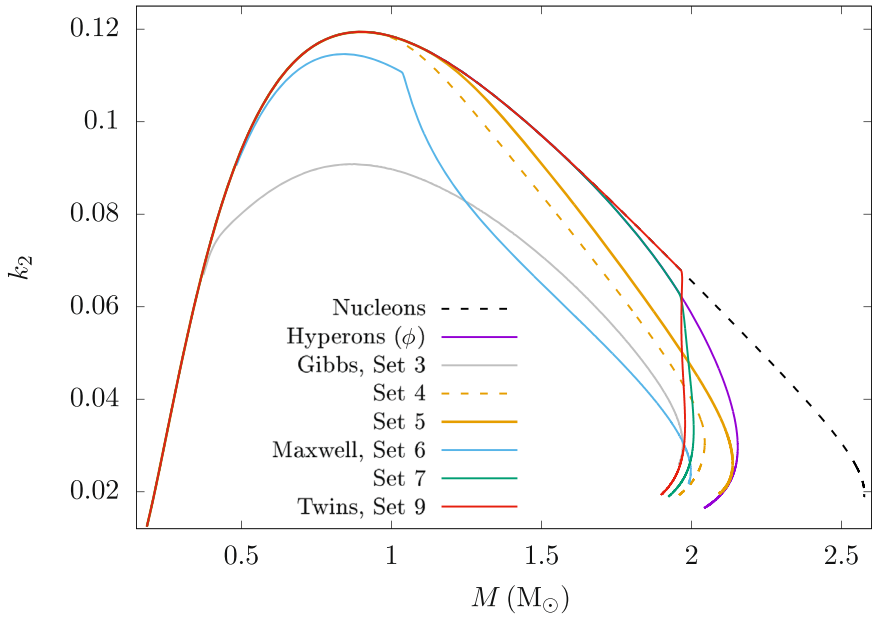

Figure 3. Same as Figure 2, plotted as a function of the mass of the star.

composition of stars and consequently their compactness. For the $1.4\,M_\odot$ star, from Table 2 one can see that the difference in radius can vary by more than 2 km when comparing hadronic and hybrid stars.

However, it is important to point out that parameterizations in Sets 3 and 6 present a reconfinement feature at high densities (Heinimann et al. 2016), which is removed by hand in Set 6, and ignored in Set 3 as the central densities of stars still allow for a mixed phase. Set 3 also presents a critical density slightly below saturation, but still above crust densities ($\rho_{b,c} = 0.138\,\mathrm{fm}^{-3}$). In particular, Sets 3 and 6 present a lower value of the bag constant, which shifts the transition point to lower chemical potentials both for Maxwell and Gibbs constructions. The early transition leads to an increase of compactness of stars and, therefore, to lower radii. As we are going to see in the next session, this has a dramatic impact on the tidal deformation of stars during mergers.

4.2. Binary Systems

In the previous section we investigated how different features in the modeling of particle interactions affect the macroscopic properties of stars. In the following, we explore the behavior of the tidal deformability when these stars are part of binary systems, according to the formalism presented in Session III. Note that, as Set 8 overlaps with Set 2, we do not display the results for this parameterization.

Figures 2 and 3 show the values of the Love number k_2 as a function of compactness and mass, respectively. One can see that the spread is little for the sets considered in this analysis, when k_2 is shown as a function of compactness in comparison

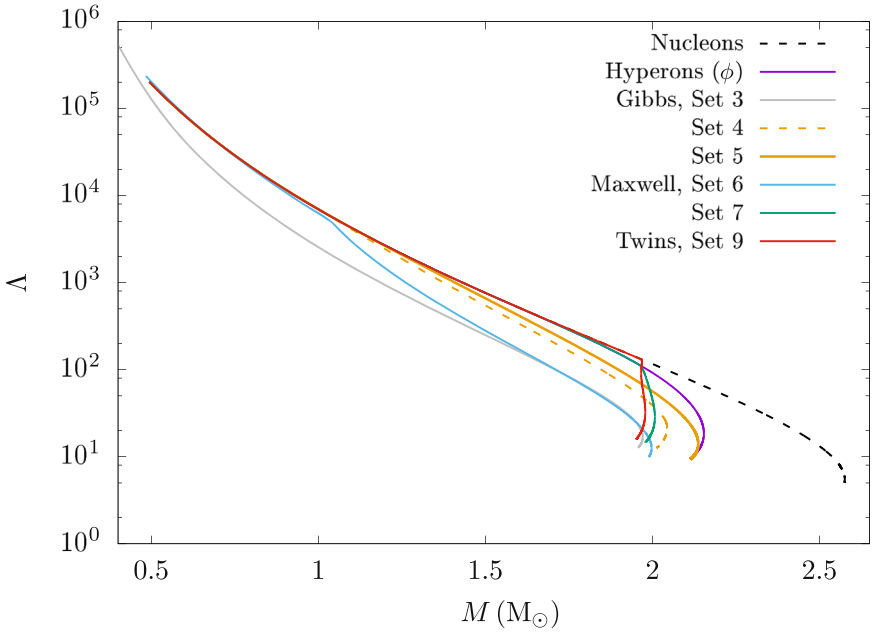

Figure 4. Dimensionless tidal deformability (vertical axis) as a function of mass for different sets of parameters.

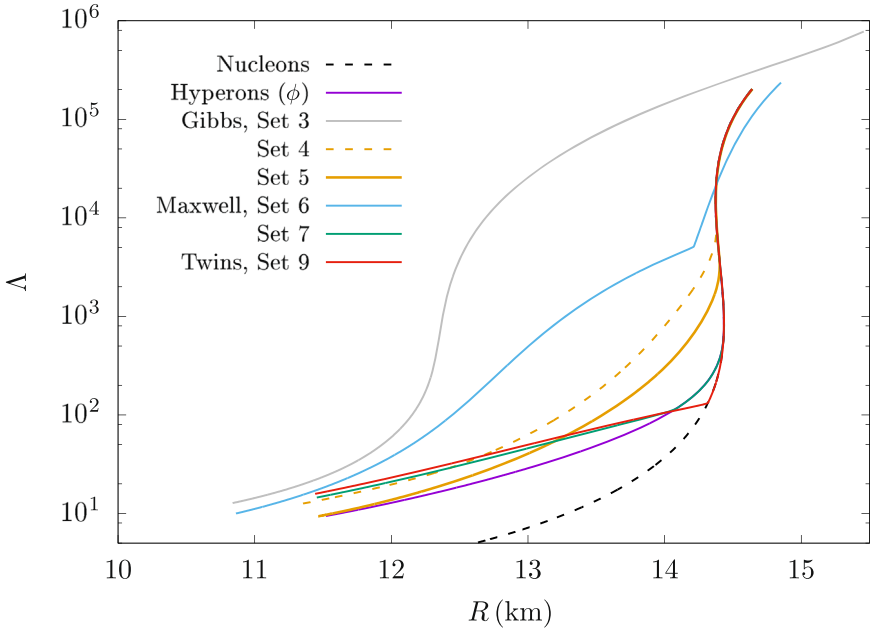

Figure 5. Same as Figure 4, as a function of the stellar radius.

to the mass of the star. The value of k_2 peaks around $1\,M_\odot$, while it is much lower at both higher and lower masses. This behavior comes from the fact that in both limits of mass, stars are more dense in the center and therefore more difficult to deform. In other words, if the mass is mostly concentrated in the center, then, regardless of how deformed the outer region could become, it will not contribute much to the quadrupole moment. If the radius is large and the mass is also uniformly distributed, then the quadrupolar contribution is also larger.

The dimensionless tidal deformability Λ, which is directly measurable from GW observations, is plotted in Figures 4 and 5 as a function of mass and radius of the stars, respectively. Our results are consistent with previous studies (Hinderer et al. 2010; Postnikov et al. 2010), and are here reported for the first time in a broad analysis of hadron-quark transition comparing Gibbs and Maxwell constructions and their respective impact on the tidal deformability of hybrid stars.

Regarding Gibbs and Maxwell constructions for hybrid stars, one can see that the range of values of Λ and k_2 lie essentially in the same region for different values of the vector interaction couplings, but branches of two sequences from the nucleonic sequence are different, being smoother for a Gibbs construction, due to the presence of a mixed phase. Also, as Gibbs transitions occur at lower densities than Maxwell, a considerable amount of quarks appears making the EoS softer and stars more compact, i.e., less deformed. More specifically, the tidal deformability λ for the set of parameters in Figure 4, for a $1.6\,M_\odot$ star, is $\lambda = 512.014$ for a nucleonic star (Set 1), whereas for a hybrid star in a Gibbs construction (Set 4) it is $\lambda = 339.51$, indicating a reduction of $\sim$34%. For a $1.8\,M_\odot$

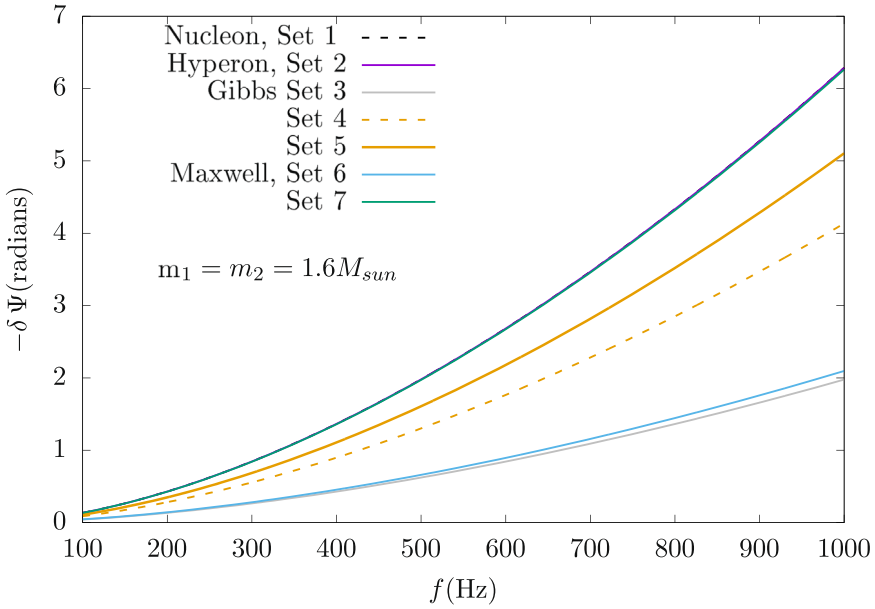

Figure 6. Total accumulated phase as a function of gravitational wave frequency for an equal mass binary system of 1.6 $M_\odot$ stars.

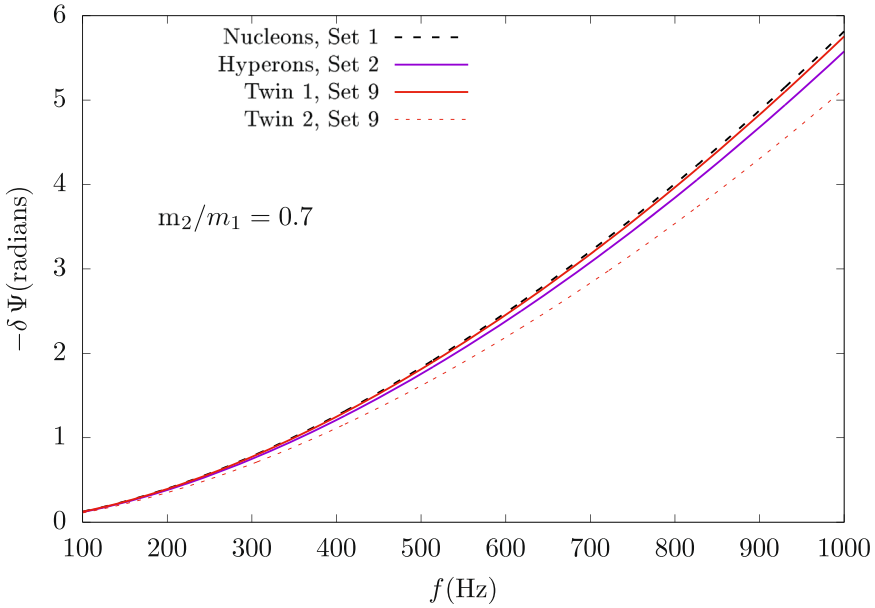

Figure 7. Same as Figure 6, but for a binary system of 1.97 $M_\odot$ stars with a companion of 1.39 $M_\odot$.

star, the same comparison leads to an even larger relative reduction of ∼48%. For the Sets 7, 8, and 9 with a Maxwell construction, the value of λ falls drastically immediately after the transition due to the sharper transition, indicating that this construction creates more compact stars in a similar mass range, in relation to Sets 1 and 2.

Furthermore, in order to study the phase lag, we plot the reduction of accumulated gravitational wave phase due to tidal interaction in Figures 6 and 7. As the innermost stable circular orbit is supposed to correspond to a phase lag frequency between 400 and 500 Hz, which can be termed as the end of the early inspiral stage (Hinderer et al. 2010), we fix the value at 450 Hz, in order to analyze each set of parameters.

For an equal mass binary where $M_1 = M_2 = 1.6\,M_\odot$, from Equation (17) we have $\tilde{\lambda} = \lambda_1 = \lambda_2$. As shown in Figure 6, we find the curves for nucleonic (Set 1), hyperonic (Set 2), and most Maxwell constructions (Sets 7, 9) essentially overlap, as the mass of the system lies only slightly above the critical one for Set 2 (only a few hyperons populate the star), and below the critical mass for the appearance of quarks for these parameterizations. However, for the Gibbs construction (Sets 3–5) and Set 6 with Maxwell, quarks are present in the core of stars starting at much lower densities. In order to quantify our results, the phase lag for a nucleonic system is 1.6614 rad, and 1.0928 rad for Set 4, with an associated difference of ∼34%. This means that the gravitational wave phase is more delayed when stars are more deformed (described with a stiffer EoS). These stars absorb more orbital energy, leading to a faster orbital decay and, hence, an earlier merger.

The weighted average of deformation $\tilde{\lambda}$ is the combined effect of both stellar deformations on the waveform, as defined in Equation (20) of Hinderer et al. (2010). In Figure 7, we use

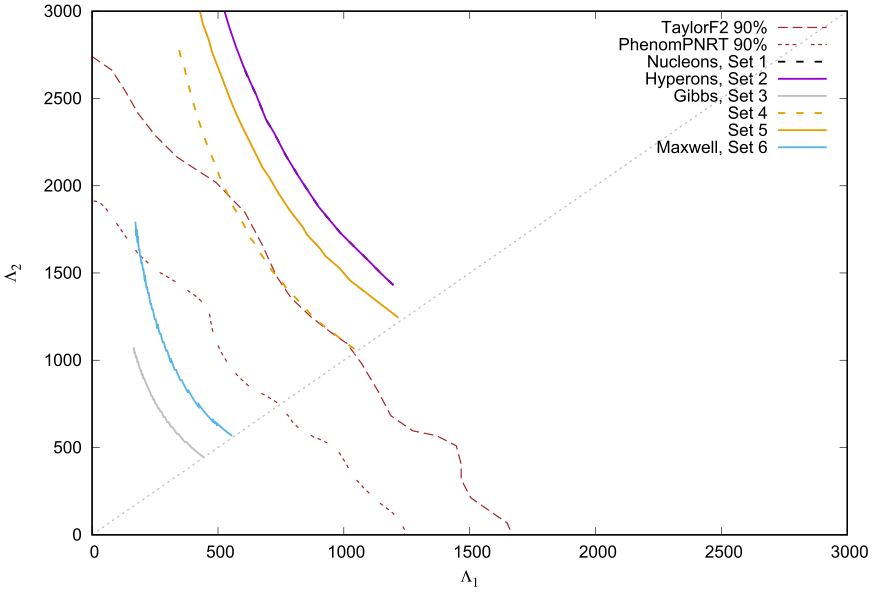

Figure 8. Tidal deformabilities associated with the individual components of the binary of GW170817.

Table 3
Properties of the 1.97 $M_\odot$ Star in a Binary System Described in Figure 7, for a Particular Binary Where $m_1 = 1.97\,M_\odot$, the Mass Ratio is $m_2/m_1 = 0.7$, and the Values for Phase Correspond to the Frequency 450 Hz

Set	$\tilde{\lambda}(10^4\,\mathrm{km}^5)$	$-\delta\Psi$ (rad)	M/R	R(km)
1	3.976	1.5365	0.138	14.32
2	3.814	1.4737	0.140	14.05
9 (Twin 1)	3.934	1.5208	0.138	14.25
9 (Twin 2)	3.510	1.3565	0.147	13.42

Note. The columns read: set of parameters, weighted average deformation $\tilde{\lambda}$, phase lag $-\delta\Psi$, compactness M/R, and radius, respectively.

this quantity for evaluating a pair of twin stars in Set 9, defining Twin-1 (nucleonic) and Twin-2 (hybrid), for a fixed mass of $M = 1.97\,M_\odot$. We take the mass ratio of the stars in the binary to $M_2/M_1 = 0.7$, for the partner star of mass, radius, and deformation of $M = 1.39\,M_\odot$, 14.43 km, and $4.313 \times 10^4\,\mathrm{km}^5$, respectively. The results for weighted average of deformation, phase lag, and radius are shown in Table 3, where we also compare with a similar mass ratio for nucleonic (Set 1) and hyperonic (Set 2) stars. From the results one can see once again that the more compact stars are less deformed and present also lower phase lag, as discussed before.

Finally, we plot the individual tidal deformabilities (Λ_1 and Λ_2) for each of the components of the binary associated with GW170817. The detected chirp mass $[\mathcal{M} = (M_1M_2)^{3/5}/(M_1 + M_2)^{1/5}]$ for this event is $1.188\,M_\odot$. We vary the high mass component (M_1) from $1.36\,M_\odot$ to $1.6\,M_\odot$ keeping the chirp mass fixed while the low mass component (M_2) being varied from $1.17\,M_\odot$ to $1.36\,M_\odot$ and plot the corresponding Λs in Figure 8. The brown dashed lines correspond to the 90% probability contour found from the event GW170817 assuming slow spinning components of the binary, being *Taylor F2* for the first analysis (Abbott et al. 2017) and *Phenom PNRT* for the latest and improved wave model (Abbott et al. 2018, 2019), which has supplied a stronger bound. This contour tells us that allowed EoS should form smaller and more compact stars than previously thought. We also find the Set 3 and Set 6 comfortably satisfy the constraint set by the event.

In both cases, we get a very early phase transition due to the smaller value of the bag constant. Hence, a large quark fraction exists even in the low mass stars in the sequences which also have smaller radii leading to very compact object formation with smaller deformabilities. The stars on Set 4 also have smaller radii due to early onset of the transition and lie very close to the contour. But, the other EoS have larger radii, therefore larger deformabilities, which place them fairly outside the constraint. Our results agree with other analyses of hybrid stars that consider only Maxwell or Gibbs constructions separately (Nandi & Char 2018; Paschalidis et al. 2018).

Another important factor for the early phase transition is the choice of a soft parameterization of the hadronic model ($\zeta = 0.085$), which is a parameterization so soft that cannot reproduce $2\,M_\odot$ stars while considering only hadronic stars (with hyperons). In this sense, our results indicate that an early phase transition supresses hyperons, making them only possible to be present in the core of hybrid stars together with quarks, in a mixed phase, when a Gibbs construction is assumed. Furthermore, as most hadronic models present a large radius for all neutron stars, our results are general and indicate that the critical mass for a phase transition should be lower than $\sim 1.4\,M_\odot$ in order to reproduce the new observational constraints from tidal deformability.

5. Conclusions

The new era of multimessenger astronomy and especially the results from GW170817 make the tidal deformability a powerful tool to constrain the equation of nuclear and quark matter at high densities. In this work, we have investigated the impact of hadron-quarks phase transitions on the properties of isolated hybrid stars, as well as hybrid stars in binary systems. We have also for the first time compared hybrid stars in Gibbs and Maxwell construction in light of the new data from GW170817.

For a fixed parameterization of the MBF model, we have changed the hadronic phase content, in order to also compare

our results with nucleonic and hyperonic stars. The quark phase was described with an MIT Bag model with vector interaction, for Gibbs and Maxwell constructions, with the vector interaction coupling and bag constant as free parameters.

We have shown that a Gibbs construction allows for a phase transition that happens at distinctly lower densities than the same set of parameters with a Maxwell construction. These results show a drastic impact on the composition of stars, making essentially the entire family of hybrid stars in a Gibbs construction contain only a thin lawyer of nucleonic matter and a core mostly composed of a mixture of phases, whereas for a Maxwell construction, only massive stars are hybrids, with a large portion of their composition consisting of hadronic matter (including hyperons) and only a small quark core. We also identify a third family of stars using a Maxwell construction that allows for the description of high mass twin stars of up to $1.97\,M_{\odot}$ (maximum mass for nucleonic) and $1.98\,M_{\odot}$ (maximum mass for hybrid).

For binary systems, we have investigated the tidal deformability and love number for stars in the different sets (different compositions). We have shown that only two among the nine sets of parameters analyzed agree with all the current observational constraints. In particular, we have shown that hybrid stars described in a Gibbs construction are more compact and less deformed because of the higher fraction of quarks inside the stars due to an early phase transition in comparison to Maxwell constructions. We have also calculated the phase lag due to tidal interaction, showing that a higher phase lag leads to faster orbital decay, being a potential tool to distinguish twin stars.

To a certain extent, Maxwell and Gibbs constructions are only simplified ways of modeling the smoothness of the interface between the phases. In reality, the transition might be more complex and, therefore, effects such as surface and Coulomb interaction can and should be incorporated explicitly when describing realistic hybrid stars (Wu & Shen 2017).

Our results show that both Gibbs and Maxwell scenarios are still possible for the description of hybrid stars, as long as the transition takes place at low enough densities. Here we stress that, although only one model was used to describe the hadronic phase, results shall remain similar for other choices of models or parameterizations, as $1.4\,M_{\odot}$ hadronic stars in general present a large radius and, therefore, do not predict a tidal deformability compatible to the GW170817 event. In this sense, we have shown that hybrid stars should have a critical mass $M_c < 1.4\,M_{\odot}$, able to allow for a high amount of quarks at the core of the stars, which ultimately reduces its radius and its tidal deformability.

Future observations of new NS-NS binary systems can bring new insights on the distinguishing of these two possible constructions. Nucleonic and hyperonic parameterization of the MBF model used in our analysis do not fulfill the tidal deformability constraints from GW170817. In this context, further investigations on the correlation of nuclear matter at saturation and tidal deformability are already being carried out.

The authors acknowledge support from NewCompstar, COST Action MP 1304, and HIC for FAIR. R.O. Gomes would like to thank V. Dexheimer and S. O. Kepler for fruitful discussions and suggestions. P. Char acknowledges support from the Navajbai Ratan Tata Trust.

ORCID iDs

R. O. Gomes https://orcid.org/0000-0003-4056-9843
P. Char https://orcid.org/0000-0001-6592-6590

References

Abbott, B. P., Abbott, R., Abbott, T. D., et al. 2017, PhRvL, 119, 161101
Abbott, B. P., Abbott, R., Abbott, T. D., et al. 2018, PhRvL, 121, 161101
Abbott, B. P., Abbott, R., Abbott, T. D., et al. 2019, PhRvX, 9, 011001
Alaverdyan, A. G., Alaverdyan, G. B., & Chiladze, A. O. 2010, IJMPD, 19, 1557
Alford, M., Braby, M., Paris, M. W., & Reddy, S. 2005, ApJ, 629, 969
Alford, M. G., Braby, M., & Mahmoodifar, S. 2010, PhRvC, 81, 025202
Alford, M. G., & Han, S. 2016, EPJA, 52, 62
Alford, M. G., Rajagopal, K., Reddy, S., & Wilczek, F. 2001, PhRvD, 64, 074017
Alford, M. G., & Sedrakian, A. 2017, PhRvL, 119, 161104
Alvarez-Castillo, D., Ayriyan, A., Benic, S., et al. 2016a, EPJA, 52, 69
Alvarez-Castillo, D., Benic, S., Blaschke, D., Han, S., & Typel, S. 2016b, EPJA, 52, 232
Alvarez-Castillo, D. E., Blaschke, D. B., Grunfeld, A. G., & Pagura, V. P. 2018, PhRvD, 99, 063010
Annala, E., Gorda, T., Kurkela, A., & Vuorinen, A. 2018, PhRvL, 120, 172703
Antoniadis, J., Freire, P. C. C., Wex, N., et al. 2013, Sci, 340, 6131
Ayriyan, A., Alvarez-Castillo, D. E., Benic, S., et al. 2017, AcPPS, 10, 799
Ayriyan, A., Bastian, N. U., Blaschke, D., et al. 2018, PhRvC, 97, 045802
Ayvazyan, N. S., Colucci, G., Rischke, D. H., & Sedrakian, A. 2013, A&A, 559, A118
Banik, S., & Bandyopadhyay, D. 2017, arXiv:1712.09760
Bednarek, I., Haensel, P., Zdunik, J. L., Bejger, M., & Manka, R. 2012, A&A, 543, A157
Bejger, M., Blaschke, D., Haensel, P., Zdunik, J. L., & Fortin, M. 2017, A&A, 600, A39
Benic, S., Blaschke, D., Alvarez-Castillo, D. E., Fischer, T., & Typel, S. 2015, A&A, 577, A40
Bhattacharyya, A., Mishustin, I. N., & Greiner, W. 2010, JPhG, 37, 025201
Bombaci, I. 2017, The Hyperon Puzzle in Neutron Stars, in Proc. 12th Int. Conf. on Hypernuclear and Strange Particle Physics (HYP2015), 17, 101002
Bombaci, I., Logoteta, D., Panda, P. K., Providência, C., & Vidaña, I. 2009, PhLB, 680, 448
Bombaci, I., Logoteta, D., Vidaña, I., & Providência, C. 2016, EPJA, 52, 58
Bombaci, I., Lugones, G., & Vidaña, I. 2007, A&A, 462, 1017
Bonanno, L., & Sedrakian, A. 2012, A&A, 539, A16
Brillante, A., & Mishustin, I. N. 2014, EL, 105, 39001
Buballa, M., Neumann, F., Oertel, M., & Shovkovy, I. 2004, PhLB, 595, 36
Burgio, G. F., Baldo, M., Sahu, P. K., & Schulze, H. J. 2002, PhRvC, 66, 025802
Burgio, G. F., Drago, A., Pagliara, G., Schulze, H. J., & Wei, J. B. 2018, ApJ, 860, 139
Burgio, G. F., & Zappalà, D. 2016, EPJA, 52, 60
Cai, B.-J., Fattoyev, F. J., Li, B.-A., & Newton, W. G. 2015, PhRvC, 92, 015802
Chatterjee, D., & Vidaña, I. 2016, EPJA, 52, 29
Chen, H., Baldo, M., Burgio, G. F., & Schulze, H. J. 2011, PhRvD, 84, 105023
Chubarian, E., Grigorian, H., Poghosyan, G. S., & Blaschke, D. 2000, A&A, 357, 968
Colucci, G., & Sedrakian, A. 2013, PhRvC, 87, 055806
Contrera, G. A., Orsaria, M., Ranea-Sandoval, I. F., & Weber, F. 2017, Int. J. Mod. Phys. Conf. Ser., 45, 1760026
Contrera, G. A., Spinella, W., Orsaria, M., & Weber, F. 2014, arXiv:1403.7415
Damour, T., & Nagar, A. 2009, PhRvD, 80, 084035
de Carvalho, S. M., Negreiros, R., Orsaria, M., et al. 2015, PhRvC, 92, 035810
de Oliveira, T., Menezes, D. P., Pinto, M. B., & Gulminelli, F. 2018, PhRvC, 97, 055205
De, S., Finstad, D., Lattimer, J. M., et al. 2018, PhRvL, 121, 091102
Demorest, P., Pennucci, T., Ransom, S., Roberts, M., & Hessels, J. 2010, Natur, 467, 1081
Denke, R. Z., & Pinto, M. B. 2013, PhRvD, 88, 056008
Dexheimer, V., Franzon, B., Gomes, R. O., et al. 2017, AN, 338, 1052
Dexheimer, V., Negreiros, R., & Schramm, S. 2015, PhRvC, 91, 055808
Dexheimer, V., & Schramm, S. 2008, ApJ, 683, 943
Dexheimer, V., Steinheimer, J., Negreiros, R., & Schramm, S. 2013, PhRvC, 87, 015804
Dexheimer, V. A., & Schramm, S. 2010, PhRvC, 81, 045201

Dimmelmeier, H., Bejger, M., Haensel, P., & Zdunik, J. L. 2009, MNRAS, 396, 2269
Dover, C. B., & Gal, A. 1985, PrPNP, 12, 171
Drago, A., Lavagno, A., & Pagliara, G. 2014, PhRvD, 89, 043014
Drago, A., Lavagno, A., Pagliara, G., & Pigato, D. 2016, EPJA, 52, 40
Drago, A., & Pagliara, G. 2018, ApJL, 852, L32
Drago, A., Pagliara, G., Popov, S. B., Traversi, S., & Wiktorowicz, G. 2018, Univ, 4, 50
Endo, T., Maruyama, T., Chiba, S., & Tatsumi, T. 2006, PThPh, 115, 337
Farhi, E., & Jaffe, R. L. 1984, PhRvD, 30, 2379
Favata, M. 2014, PhRvL, 112, 101101
Fernandez, F., Mesquita, A., Razeira, M., & Vasconcellos, C. A. Z. 2010, IJMPD, 19, 1545
Flanagan, E. E., & Hinderer, T. 2008, PhRvD, 77, 021502
Fonseca, E., Pennucci, T. T., Ellis, J. A., et al. 2016, ApJ, 832, 167
Fortin, M., Avancini, S. S., Providência, C., & Vidaña, I. 2017, PhRvC, 95, 065803
Fortin, M., Providência, C., Raduta, A. R., et al. 2016, PhRvC, 94, 035804
Fraga, E. S., Kurkela, A., & Vuorinen, A. 2014, ApJL, 781, L25
Fraga, E. S., Pisarski, R. D., & Schaffner-Bielich, J. 2001, PhRvD, 63, 121702
Franzon, B., Dexheimer, V., & Schramm, S. 2015, MNRAS, 456, 2937
Franzon, B., Gomes, R. O., & Schramm, S. 2016, MNRAS, 463, 571
Garcia, A. F., & Pinto, M. B. 2013, PhRvC, 88, 025207
Glendenning, N. K. 1992, PhRvD, 46, 1274
Glendenning, N. K., Pei, S., & Weber, F. 1997, PhRvL, 79, 1603
Glendenning, N. K., & Weber, F. 2001, ApJL, 559, L119
Gomes, R. O., Dexheimer, V., Schramm, S., & Vasconcellos, C. A. Z. 2015, ApJ, 808, 8
Haidenbauer, J., Meißner, U. G., Kaiser, N., & Weise, W. 2017, EPJA, 53, 121
Heinimann, O., Hempel, M., & Thielemann, F.-K. 2016, PhRvD, 94, 103008
Heiselberg, H., Pethick, C. J., & Staubo, E. F. 1993, PhRvL, 70, 1355
Hempel, M., Pagliara, G., & Schaffner-Bielich, J. 2009, PhRvD, 80, 125014
Hinderer, T. 2008, ApJ, 677, 1216
Hinderer, T., Lackey, B. D., Lang, R. N., & Read, J. S. 2010, PhRvD, 81, 123016
Ippolito, N., Ruggieri, M., Rischke, D., Sedrakian, A., & Weber, F. 2008, PhRvD, 77, 023004
Jiang, W.-Z., Li, B.-A., & Chen, L.-W. 2012, ApJ, 756, 56
Klähn, T., & Fischer, T. 2015, ApJ, 810, 134
Klähn, T., Lastowiecki, R., & Blaschke, D. B. 2013, PhRvD, 88, 085001
Krastev, P. G., & Li, B.-A. 2018, arXiv:1801.04620
Kumar, B., Biswal, S. K., & Patra, S. K. 2017, PhRvC, 95, 015801
Lenzi, C. H., & Lugones, G. 2012, ApJ, 759, 57
Li, A., Zuo, W., & Peng, G. X. 2015, PhRvC, 91, 035803
Lim, Y., Kwak, K., Hyun, C. H., & Lee, C.-H. 2014, PhRvC, 89, 055804
Love, A. E. H. 1909, RSPSA, 82, 73
Lugones, G., & Grunfeld, A. G. 2017, PhRvC, 95, 015804
Lugones, G., Grunfeld, A. G., & Al Ajmi, M. 2013, PhRvC, 88, 045803
Malik, T., Alam, N., Fortin, M., et al. 2018, PhRvC, 98, 035804
Mariani, M., Orsaria, M., & Vucetich, H. 2017, IJMPS, 45, 1760041
Marques, M., Oertel, M., Hempel, M., & Novak, J. 2017, PhRvC, 96, 045806
Maruyama, T., Chiba, S., Schulze, H.-J., & Tatsumi, T. 2007, PhRvD, 76, 123015
Maruyama, T., Chiba, S., Schulze, H.-J., & Tatsumi, T. 2008, PhLB, 659, 192
Masuda, K., Hatsuda, T., & Takatsuka, T. 2013, ApJ, 764, 12
McLerran, L., & Reddy, S. 2018, PhRvL, 122, 122701
Menezes, D. P., Panda, P. K., & Providência, C. 2005, PhRvC, 72, 035802
Menezes, D. P., Pinto, M. B., Castro, L. B., Costa, P., & Providência, C. 2014, PhRvC, 89, 055207
Mesquita, A., Razeira, M., Vasconcellos, C. A. Z., & Fernandez, F. 2010, IJMPD, 19, 1549
Mishra, A., Kumar, A., Sanyal, S., Dexheimer, V., & Schramm, S. 2010, EPJA, 45, 169
Mishra, R. N., Sahoo, H. S., Panda, P. K., Barik, N., & Frederico, T. 2016, PhRvC, 94, 035805
Miyatsu, T., Kambe, T., & Saito, K. 2017, PoS, INPC2016, 135
Most, E. R., Weih, L. R., Rezzolla, L., & Schaffner-Bielich, J. 2018, PhRvL, 120, 261103
Muto, T., Maruyama, T., & Tatsumi, T. 2015, AcASn, 56, 43
Nandi, R., & Char, P. 2018, ApJ, 857, 12
Oertel, M., Providência, C., Gulminelli, F., & Raduta, A. R. 2015, JPhG, 42, 075202
Page, D., Geppert, U., & Weber, F. 2006, NuPhA, 777, 497
Palhares, L. F., & Fraga, E. S. 2010, PhRvD, 82, 125018
Paschalidis, V., Yagi, K., Alvarez-Castillo, D., Blaschke, D. B., & Sedrakian, A. 2018, PhRvD, 97, 084038
Pereira, J. P., Flores, C. V., & Lugones, G. 2018, ApJ, 860, 12
Pereira, R. C., Costa, P., & Providência, C. 2016, PhRvD, 94, 094001
Pinto, M. B., Koch, V., & Randrup, J. 2012, PhRvC, 86, 025203
Pons, J. A., Steiner, A. W., Prakash, M., & Lattimer, J. M. 2001, PhRvL, 86, 5223
Postnikov, S., Prakash, M., & Lattimer, J. M. 2010, PhRvD, 82, 024016
Rabhi, A., Pais, H., Panda, P. K., & Providência, C. 2009, JPhG, 36, 115204
Radice, D., Perego, A., Zappa, F., & Bernuzzi, S. 2018, ApJL, 852, L29
Raithel, C., Özel, F., & Psaltis, D. 2018, ApJL, 857, L23
Ranea-Sandoval, I. F., Han, S., Orsaria, M. G., et al. 2016, PhRvC, 93, 045812
Regge, T., & Wheeler, J. A. 1957, PhRv, 108, 1063
Restrepo, T. E., Macias, J. C., Pinto, M. B., & Ferrari, G. N. 2015, PhRvD, 91, 065017
Rueda, J. A., Ruffini, R., Wang, Y., et al. 2018, JCAP, 1810, 006
Schaffner, J., Dover, C. B., Gal, A., et al. 1994, AnPhy, 235, 35
Schaffner, J., & Mishustin, I. N. 1996, PhRvC, 53, 1416
Schramm, S., Dexheimer, V., & Negreiros, R. 2016, EPJA, 52, 14
Schurhoff, T., Schramm, S., & Dexheimer, V. 2010, ApJL, 724, L74
Shao, G. Y., Colonna, M., Di Toro, M., Liu, B., & Matera, F. 2012, PhRvD, 85, 114017
Shao, G. Y., Colonna, M., Di Toro, M., Liu, Y. X., & Liu, B. 2013, PhRvD, 87, 096012
Shuryak, E. 2009, PrPNP, 62, 48
Sotani, H., & Tatsumi, T. 2015, MNRAS, 447, 3155
Stiele, R., & Schaffner-Bielich, J. 2016, PhRvD, 93, 094014
Sun, T.-T., Xia, C.-J., Zhang, S.-S., & Smith, M. S. 2018, ChPhC, 42, 025101
Tews, I., Margueron, J., & Reddy, S. 2018, PhRvC, 98, 045804
Tolos, L., Centelles, M., & Ramos, A. 2017a, ApJ, 834, 3
Tolos, L., Centelles, M., & Ramos, A. 2017b, PASA, 34, e065
Torres, J. R., Gulminelli, F., & Menezes, D. P. 2017, PhRvC, 95, 025201
Vidaña, I. 2016, JPhCS, 668, 012031
Voskresensky, D. N., Yasuhira, M., & Tatsumi, T. 2003, NuPhA, 723, 291
Weissenborn, S., Chatterjee, D., & Schaffner-Bielich, J. 2012, NuPhA, 881, 62
Weissenborn, S., Sagert, I., Pagliara, G., Hempel, M., & Schaffner-Bielich, J. 2011, ApJL, 740, L14
Whittenbury, D. L., Matevosyan, H. H., & Thomas, A. W. 2016, PhRvC, 93, 035807
Wu, X., & Shen, H. 2017, PhRvC, 96, 025802
Yamamoto, Y., Furumoto, T., Yasutake, N., & Rijken, T. A. 2016, EPJA, 52, 19
Yasutake, N., Burgio, G. F., & Schulze, H. J. 2011, PAN, 74, 1502
Yasutake, N., Chen, H., Maruyama, T., & Tatsumi, T. 2016, JPhCS, 665, 012068
Yasutake, N., & Kashiwa, K. 2009, PhRvD, 79, 043012
Yasutake, N., Lastowiecki, R., Benic, S., et al. 2014, PhRvC, 89, 065803
Zacchi, A., Hanauske, M., & Schaffner-Bielich, J. 2016, PhRvD, 93, 065011
Zdunik, J. L., Bejger, M., Haensel, P., & Gourgoulhon, E. 2006, A&A, 450, 747
Zhao, X.-F. 2015, PhRvC, 92, 055802
Zhou, E.-P., Zhou, X., & Li, A. 2018, PhRvD, 97, 083015
Zhu, Z.-Y., Li, A., Hu, J.-N., & Sagawa, H. 2016, PhRvC, 94, 045803
Zhu, Z.-Y., Zhou, E.-P., & Li, A. 2018, ApJ, 862, 98